Journal of *Marine Science and Engineering*

MDPI

Article

Numerical Simulation Study on Hydrodynamic Characteristics of Offshore Floating Photovoltaics

Shuting Sui [1], Lu Cao [2,*], Yun Gao [2], Zhongyan Huo [2] and Qi Chen [2]

[1] School of Naval Architecture and Marine, Zhejiang Ocean University, Zhoushan 316021, China; suishuting111@163.com
[2] School of Marine Engineering Equipment, Zhejiang Ocean University, Zhoushan 316021, China; zjgaoyun@163.com (Y.G.); huozhongyan@zjou.edu.cn (Z.H.); cq15088871486@163.com (Q.C.)
* Correspondence: lucaogh@zjou.edu.cn

Abstract: With the development of renewable energy and the utilization of marine resources, large-scale offshore floating photovoltaics have gradually attracted widespread attention. In order to develop offshore floating photovoltaics and promote sustainable development, it has become necessary to explore the hydrodynamic characteristics of floating photovoltaic units and floating arrays. In this work, based on the viscous flow theory, the Computational Fluid Dynamics (CFD) and the discrete element method (DEM) methods are used to analyze the hydrodynamics of the floating body unit of offshore floating photovoltaics. The influencing factors include mooring length, mooring radius, and floating unit length. In addition, the hydrodynamic performance of the floating body unit and the floating body array under different wave heights and periods is also discussed to explore the influence of environmental loads on the floating body unit and the floating body array. The results indicate that the mooring tension exhibits an opposite trend with the surge and heave motions when the mooring line length and radius are varied. The motion is found to be more pronounced when the floating body unit length is 0.4 times the wavelength. The heave motion of the floating body unit exhibits a strong linear relationship with wave height, increasing by 0.01 m for every 0.015 m increase in wave height. The motion of the floating body units on both sides connected to the mooring lines decreases as the array length increases.

Keywords: offshore floating photovoltaic; mooring; hydrodynamic; numerical wave flume; CFD

check for updates

Academic Editor: Giuseppe Giorgi

Received: 9 November 2024
Revised: 11 January 2025
Accepted: 13 January 2025
Published: 15 January 2025

Citation: Sui, S.; Cao, L.; Gao, Y.; Huo, Z.; Chen, Q. Numerical Simulation Study on Hydrodynamic Characteristics of Offshore Floating Photovoltaics. *J. Mar. Sci. Eng.* **2025**, *13*, 142. https://doi.org/10.3390/jmse13010142

Copyright: © 2025 by the authors. Licensee MDPI, Basel, Switzerland. This article is an open access article distributed under the terms and conditions of the Creative Commons Attribution (CC BY) license (https://creativecommons.org/licenses/by/4.0/).

1. Introduction

With the development and utilization of renewable energy, green industries such as solar photovoltaics have gained significant attention [1]. Photovoltaic power generation offers several advantages, including a simple power generation process, no fuel consumption, independence from regional and altitude constraints, and minimal pollution, making it a crucial component of sustainable development [2,3]. A floating photovoltaic system is primarily composed of a photovoltaic system, a floating system, and a mooring system [4,5]. The floating system is typically comprised of multiple floating body units that provide buoyancy and support for the photovoltaic system. Currently, floating photovoltaics are mainly deployed in inland waters such as lakes and reservoirs. The floating photovoltaic (FPV) systems offer promising solutions to long-term energy demands, as they cover water bodies instead of valuable land resources used for installation [6–8]. As a large marine nation, China is characterized by a vast sea area, a long coastline, and rich marine resources.

It is regarded as having great potential for development and providing superior basic conditions for the development of large-scale offshore floating photovoltaics. The development of offshore floating photovoltaic systems is considered a vital strategy for renewable energy utilization and plays a crucial role in advancing China's sustainable development goals [9]. However, the substantial environmental loads in the marine environment are found to place higher demands on the floating and mooring systems of offshore floating photovoltaics.

China's offshore floating photovoltaic technology is in the early stages of development. At present, offshore floating photovoltaic structures mainly include multi-module connected multi-floating body types and flexible floating types [10]. In recent years, multi-module, multi-float photovoltaic structures have attracted significant attention in offshore photovoltaic research due to their ease of transportation, rapid assembly, and scalability [11–13]. This form of structure requires further research on the floating structure and mooring system to prevent the failure of the offshore floating photovoltaic system. The research on offshore photovoltaics primarily utilizes potential flow theory. Based on the potential flow theory, Ji C [14], Jiang Z [15], and Wang B [16] discussed the hydrodynamic characteristics of the photovoltaic system by studying the connectors of the floating body system. Y Li [17], Xu W [18], and Tang Y [19], applying potential flow theory, studied the mooring tension and dynamic response of offshore photovoltaic systems with various floating structures. Similarly, Du J [20], also based on potential flow theory, designed six mooring models for offshore floating photovoltaics in ultra-shallow waters, comparing the advantages and disadvantages of these systems. Yu L [21] investigated the gravity anchor system for floating photovoltaics, providing new insights into their anchoring mechanisms.

Currently, numerous numerical simulations explore the interaction between waves and structures [22–24], yet relatively few studies focus on the response of floating bodies and mooring systems under viscous flow conditions. Domínguez J M [25] investigated the mooring tension and dynamic response of mooring pontoons based on the coupling of DualSPHysics and MoorDyn (Lumped-Mass Mooring Dynamics). Chen H [26] utilized OpenFOAM® and MoorDyn coupling to study the changes of wave height, floating body motion, and mooring tension. However, the accuracy of the traditional SPH method in simulating the free surface boundary is low, and the motion state of the fluid cannot be well simulated. When OpenFOAM® simulates the motion of a floating body, it generally uses two methods: overlapping grid [27,28] and dynamic grid [29,30]. The computational efficiency of the overlapping grid is slow, and the dynamic grid cannot calculate the large deformation motion of the object. In STAR-CCM+, the catenary model for mooring systems allows for the setting of parameters such as unit mass, length, and stiffness. This approach can accommodate taut mooring simulations; however, when the length of the catenary is sufficiently long to reach the bottom of the flume, the system may penetrate the flume model, as shown in Figure 1a, preventing accurate simulation of the mooring line touching the bottom and thus affecting the precision of numerical results. The application of DEM to simulate mooring system can directly solve and configure the detailed parameters of mooring, such as Young 's modulus, diameter, stiffness, density, and length. It can not only avoid the problem of mooring penetration at the bottom, as shown in Figure 1, but also consider some special problems, such as local problems that cannot be considered by the lumped-mass method [31].

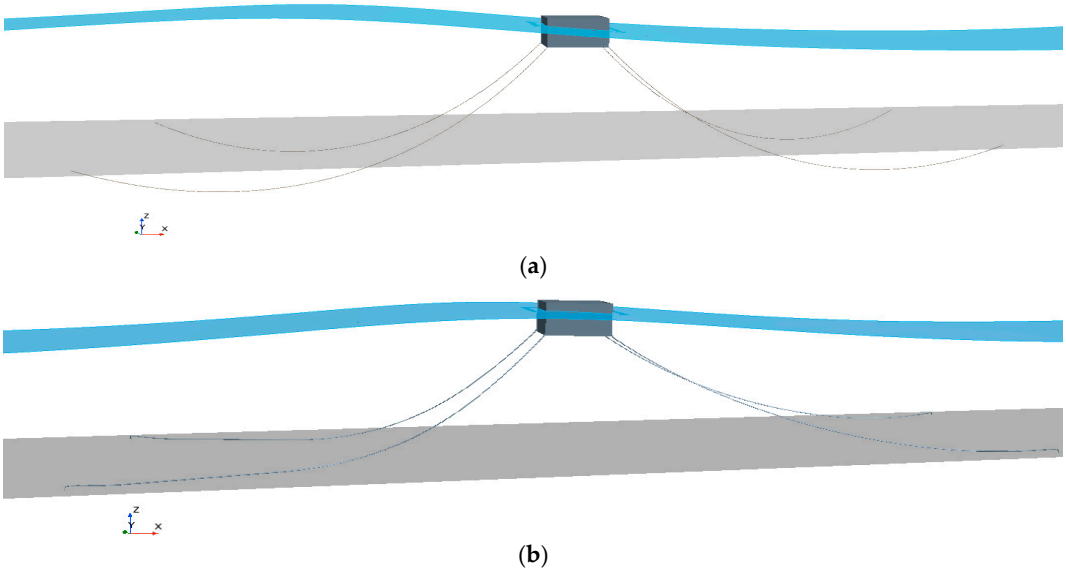


Figure 1. Comparison diagram of catenary and DEM mooring: (**a**) catenary, (**b**) DEM mooring.

Previous research on photovoltaic panels has predominantly concentrated on fixed installation methods and numerical simulations based on potential flow theory. However, the method based on potential flow theory is limited in accurately representing phenomena such as the green water effect and wave breaking. In this paper, STAR-CCM+2402 software is utilized to establish a numerical wave flume based on the Navier–Stokes (RANS) model, while the DEM is employed to simulate the mooring system. The research focuses on the hydrodynamic characteristics of a single row of floating body arrays, particularly the motion behavior of individual floating bodies within the array. These findings hold fundamental significance for the design and implementation of large-scale photovoltaic arrays and establish a strong foundation for the further advancement of array-type floating photovoltaic systems.

The structure of this paper is organized as follows: Section 1 provides an introduction to the numerical model utilized in this study. Section 2 discusses the numerical model and its validation, including a comparison between the mooring forces, surge, heave, and pitch motions obtained from the numerical and experimental results. Section 3 analyzes the effects of various parameters, including wave height, wave period, mooring length, radius, floating body unit length, and the number of floating body units. Finally, the conclusions of the study are presented in Section 4.

2. Numerical Model

2.1. Governing Equations

The flow of viscous fluids, considered incompressible, follows the principles of mass conservation, momentum conservation, and energy conservation. In this study, the energy-conservation equation is neglected due to the disregard for energy conversion caused by temperature changes. The flow of viscous fluids satisfies the Navier–Stokes (N-S) equations [32,33].

$$\frac{\partial u}{\partial x} + \frac{\partial v}{\partial y} + \frac{\partial w}{\partial z} = 0 \tag{1}$$

$$\frac{\partial u}{\partial t} + u\frac{\partial u}{\partial x} + v\frac{\partial u}{\partial y} + w\frac{\partial u}{\partial z} = -\frac{1}{\rho}\frac{\partial p}{\partial x} + \frac{\mu}{\rho}\left(\frac{\partial^2 u}{\partial x^2} + \frac{\partial^2 u}{\partial y^2} + \frac{\partial^2 u}{\partial z^2}\right) + f_x \tag{2}$$

$$\frac{\partial v}{\partial t} + u\frac{\partial v}{\partial x} + v\frac{\partial v}{\partial y} + w\frac{\partial v}{\partial z} = -\frac{1}{\rho}\frac{\partial p}{\partial y} + \frac{\mu}{\rho}\left(\frac{\partial^2 v}{\partial x^2} + \frac{\partial^2 v}{\partial y^2} + \frac{\partial^2 v}{\partial z^2}\right) + f_y \tag{3}$$

$$\frac{\partial w}{\partial t} + u\frac{\partial w}{\partial x} + v\frac{\partial w}{\partial y} + w\frac{\partial w}{\partial z} = -\frac{1}{\rho}\frac{\partial p}{\partial z} + \frac{\mu}{\rho}\left(\frac{\partial^2 w}{\partial x^2} + \frac{\partial^2 w}{\partial y^2} + \frac{\partial^2 w}{\partial z^2}\right) + f_z \tag{4}$$

where u, v, and w are the velocity components in the X, Y, and Z directions in the Cartesian coordinate system, t is the time, ρ is the fluid density, p is the pressure, μ is the dynamic viscosity coefficient, and f_x, f_y, and f_z are the components of the unit mass force in the X, Y, and Z directions, respectively. The fluid in this paper is water, so $\mu = 1.01 \times 10^{-3}$. For the particle discrete phase, DEM is applied. In this model, DEM particles are used as mooring, and only the drag force, pressure gradient force, self-gravity, and contact force between DEM particles are considered.

The particle motion is governed by the momentum conservation equation:

$$m_p\frac{dv_p}{dt} = F_d + F_p + F_g + F_c \tag{5}$$

where v_p is the instantaneous velocity of the particles, m_p is the particle mass, F_d is the drag force, F_p is the pressure gradient force of the particles, F_g is the self-gravity of the particles, and F_c is the contact force between the particles.

The drag force can be expressed as follows:

$$F_d = \frac{1}{2}C_d\rho A_p|v_s|v_s \tag{6}$$

where ρ represents the density of the continuous phase, A_p denotes the projected area of the particle, and $v_s = v - v_p$ indicates the slip velocity of the particle. C_d is the drag coefficient of the particle.

In this paper, cylindrical particles are utilized, and therefore, the Clift drag coefficient method, specifically designed for cylindrical particles, is employed. See the STAR-CCM+ instructions for details.

$$Re_p \le 5 : C_d = 9.689Re_p^{-0.78}\left(1 + 0.147{Re_p}^{0.82}\right) \tag{7}$$

$$5 < Re_p \le 40 : C_d = 9.689Re_p^{-0.78}\left(1 + 0.227{Re_p}^{0.55}\right) \tag{8}$$

$$40 < Re_p \le 400 : C_d = 9.689Re_p^{-0.78}\left(1 + 0.0838{Re_p}^{0.82}\right) \tag{9}$$

$$Re_p > 400 : C_d = 0.99\gamma^{-0.12}E^{-0.08} \tag{10}$$

where γ is the ratio of particle density to fluid density. E is the length–width ratio.

Pressure gradient force:

$$\mathrm{F_p} = -\mathrm{V_p}\nabla\mathrm{p} \tag{11}$$

where $\mathrm{V_p}$ denotes the volume of the particles and $\nabla\mathrm{p}$ denotes the pressure gradient in the continuous phase. Contact force between particles:

$$\mathrm{F_c} = \mathrm{F_n}\mathrm{n} + \mathrm{F_t}\mathrm{t} \tag{12}$$

where $\mathrm{F_n}$ is the normal force amplitude and $\mathrm{F_t}$ is the tangential force amplitude.

2.2. VOF Model

The Volume of Fluid (VOF) model is a simplified multiphase model used to simulate the flow of immiscible fluids on numerical grids and can resolve the interfaces between different phases.

In this study, the gas–liquid two-phase flow model is used to solve the motion of air and water, and the VOF method is used to capture the interface between water and air. The transport equation for the VOF method is expressed as follows:

$$\frac{\partial \alpha}{\partial t} + \frac{\partial (u\alpha)}{\partial x} + \frac{\partial (v\alpha)}{\partial y} + \frac{\partial (w\alpha)}{\partial z} = 0 \tag{13}$$

where α is the volume fraction function, which represents the ratio of the volume occupied by the fluid in the grid cell to the volume of the grid cell. α = 1 indicates that the cell is filled with water, α = 0 indicates that it is filled with air, and α between 0 and 1 indicates a mixture of air and water in the cell.

2.3. Boundary Wave-Generation Method

In this study, wave generation is achieved by specifying the fluid velocity in the x and z directions, along with the instantaneous wave surface elevation. Based on the mechanical characteristics of marine structures, a comparison between theoretical calculations and flume test results suggests that the Stokes fifth-order wave theory provides greater accuracy compared to lower-order wave theories [34]. The velocity and wave surface equations at the wave-making boundary satisfy the following conditions:

X-direction velocity:

$$u_x = c \sum_{n=1}^{5} n\lambda_n \cosh[nk(z+d)] \cos[n(kx - \omega t)] \tag{14}$$

Z-direction velocity:

$$u_z = c \sum_{n=1}^{5} n\lambda_n \sinh[nk(z+d)] \sin[n(kx - \omega t)] \tag{15}$$

Wave surface equation:

$$\eta = \frac{1}{k} \sum_{n=1}^{5} \lambda_n \cos[n(kx - \omega t)] \tag{16}$$

where ω, d, and k are the circular frequency, water dept, and wave number, c = coshkd, and s = sinhkd.

3. Results and Discussion

3.1. Validation of Numerical Model

Although the DEM method can visually simulate mooring, its effectiveness requires verification. To assess the accuracy of the numerical simulation model and DEM mooring, we refer to the research of Liang [35] and Chen [36]. Figure 2 shows a numerical wave flume based on Liang's experiment, with dimensions of 13 m in length, 0.8 m in width, and 0.9 m in height. Liang employed the wave slope approach to address wave reflection in the wave-abatement zone, whereas we utilized the force wave elimination technique to mitigate wave reflection within the numerical model. The location of x = 0 is located at the left boundary. A box measuring 0.745 m in length, 0.5 m in width, 0.28 m in height, and 0.16 m in depth is included. The water depth is 0.6 m, wave height is 0.1 m, and the period is 1.4 s. The mooring length is 0.809 m, and the stiffness is 2360 N/m. Four wave height meters (G1, G2, G3, G4) were set up to monitor the wave height. The wave height meters were placed at x = 2.815 m, x = 3.5 m, x = 9.5 m, and x = 10 m, respectively, as shown in Figure 2.

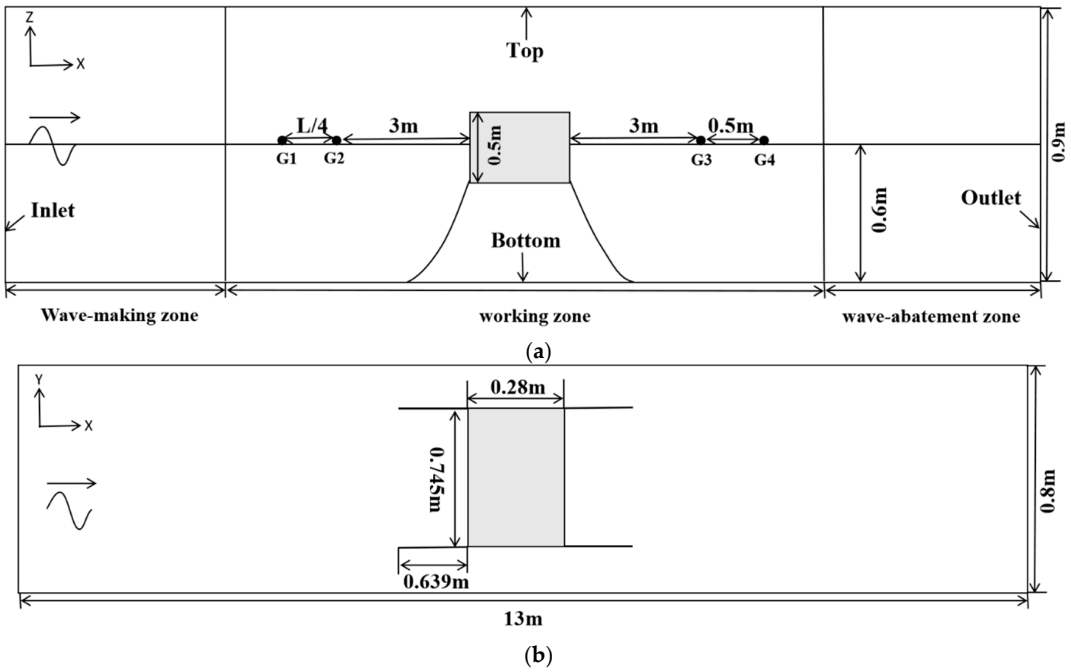


Figure 2. Numerical wave flume arrangement: (**a**) side view, (**b**) vertical view.

3.1.1. Grid Convergence Verification

To verify the accuracy of wave making in the numerical flume, a grid convergence analysis is first conducted, using three grid types (coarse, medium, and fine) to compare the simulation results. The detailed grid parameters are provided in Table 1.

Table 1. Mesh parameters.

Grid Name	Fiducial Value (m)	Total Number of Grids
fine	0.2	1,100,000
medium	0.15	400,000
coarse	0.1	17,000

Figure 3 shows the wave duration curve of the wave altimeter at x = 6.5 m for a wave height of 0.1 m and a period of 1.4 s. As shown in Figure 3, the coarse grid yields a significantly higher peak value compared to the medium and fine grids, with the difference between the medium and fine grids at the peak being only 0.00002 m. To balance calculation time and accuracy, the medium grid is chosen for the subsequent simulations.

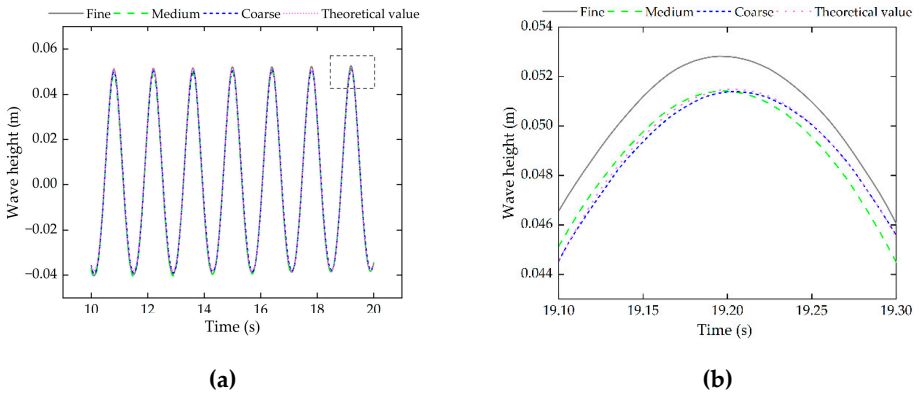


Figure 3. Wave duration curves under different grids: (**a**) wave duration curve diagram, (**b**) local wave duration curve diagram.

3.1.2. Time Step Convergence Verification

In this study, a second-order time discretization scheme is used. Since the time step significantly impacts both the accuracy of the results and the convergence of residuals, it is necessary to verify its convergence. The numerical results for three different time steps—0.001 s, 0.005 s, and 0.01 s—are compared. Figure 4 shows the free surface duration curve of the wave altimeter at $x = 0$ with the selected grid. As seen in Figure 4, the wave phase difference between 0.01 s and 0.005 s is 0.1 s, and between 0.005 s and 0.001 s, it is 0.002 m. Considering both calculation efficiency and accuracy, a time step of 0.005 s has been selected.

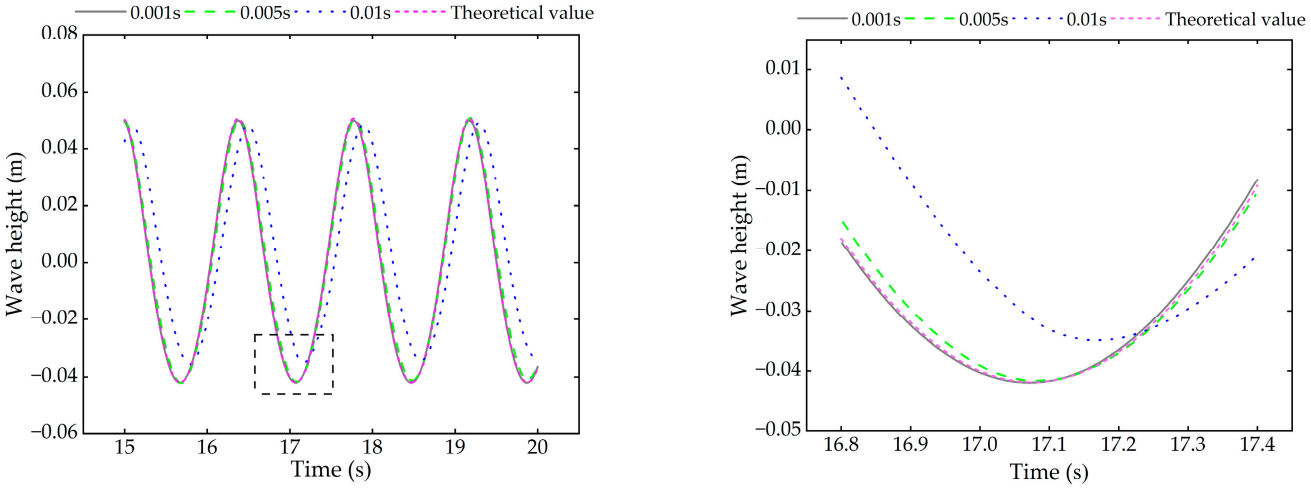


Figure 4. Wave duration curves with different time steps: (**a**) wave duration curve diagram, (**b**) local wave duration curve diagram.

3.1.3. Validation of Test and Simulation Results

Figure 5 shows the time-history curves of mooring tension. As the waves propagate, the mooring tension on both the seaward and leeward sides exhibits periodic variations, which are in good agreement with the experimental results. The maximum error for the wave-facing side is 10.7%, with an average error of 8.2%. For the leeward side, the maximum error is 11.2%, and the average error is 6.8%. The differences between the numerical simulations and experimental results are mainly caused by wave elimination conditions in the numerical model, which result in the reduction of the positive effect of boundary-reflected waves on the seaward side and the negative effect on the leeward side. As a result, a smaller mooring tension on the seaward side and larger forces on the leeward side are observed, compared to the experimental data.

Figure 6 illustrates the time-history curves for the surge, heave, and pitch motions of the structure. The maximum errors for these motions are 10.2%, 9.8%, and 6.3%, which fall within a reasonable range, indicating good correlation between the numerical and experimental results. Therefore, the numerical model established in this study can effectively simulate the floating structure and mooring system of offshore floating photovoltaic systems.

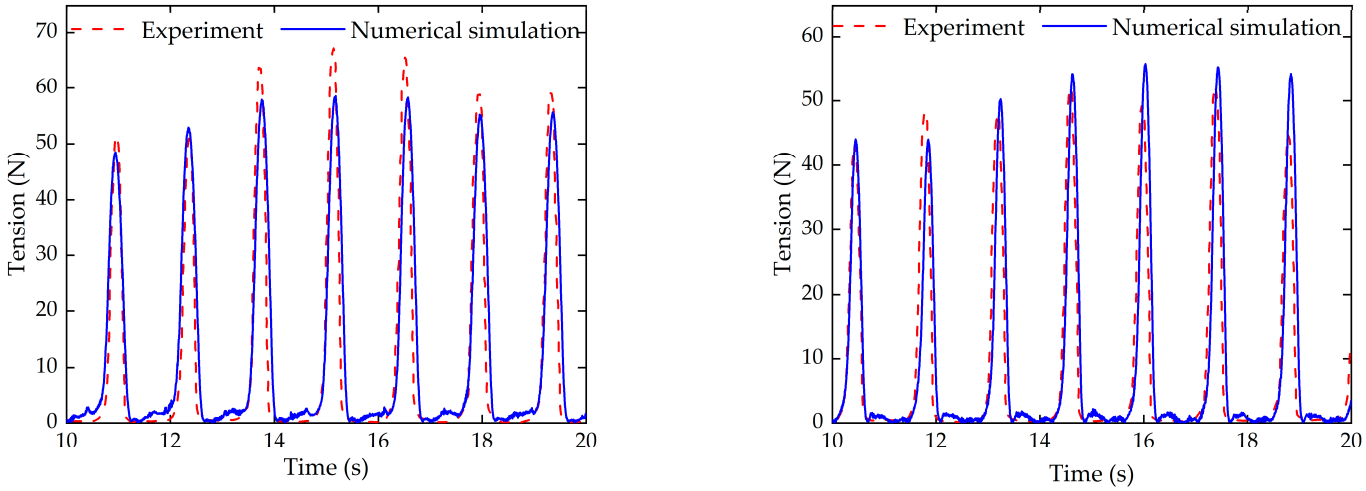


Figure 5. Mooring tension duration curve: (**a**) seaward line, (**b**) leeward line.

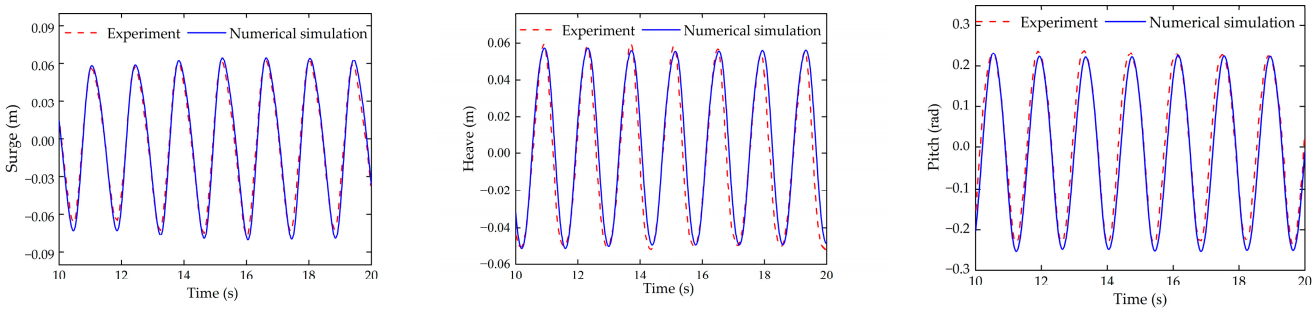


Figure 6. Three-degree-of-freedom motion duration curve of the square box: (**a**) surge, (**b**) heave, (**c**) pitch.

3.2. Numerical Simulation of Offshore Floating Photovoltaics

3.2.1. Working Condition Design

The floating body unit model used in this study is presented in Figure 7, with specific parameters provided in Table 2. In this paper, a semi-tensioned mooring line is employed. Since JM Domínguez's test utilized a semi-tensioned mooring line, the mooring parameters were adopted based on JM Domínguez's test [25]. The flume has dimensions of 10 m in length, 0.6 m in width, and 0.8 m in height. Based on ERA5 data, the annual average wave height in the Bohai Sea, Yellow Sea, and East China Sea ranges from 0.5 m to 1.8 m, while the annual average wave period in the East China Sea is between 5 s and 8 s [37]. The selected wave heights for the simulations are 0.75 m, 1.125 m, and 1.5 m, with periods of 5 s, 6 s, 7 s, and 8 s. The Froude law is adopted; the ratio is 1:25. Additionally, a typical wave scenario caused by light breezes, with a wave height between 0.1 m and 0.5 m, is considered, with a selected height of 0.375 m. The wave conditions are summarized in Table 3.

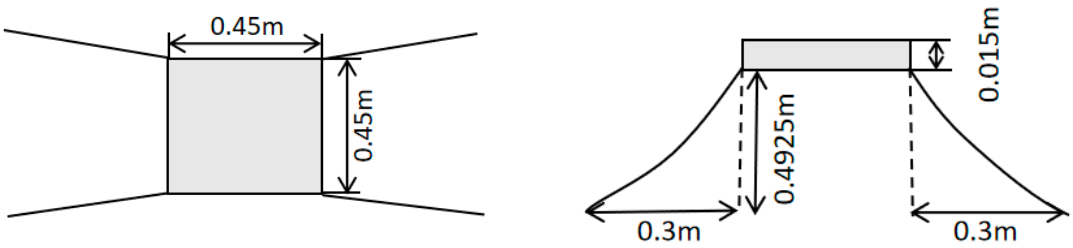


Figure 7. Schematic diagram of floating body unit size: (**a**) vertical view, (**b**) side view.

Table 2. Model parameters.

Floating Body Unit			Mooring Parameters				
Length (*L*)/(m)	**Width (*W*)/(m)**	**Height (*B*)/(m)**	**Length (*l*)/(m)**	**Radius (*r*)/(m)**	**Density (ρ)/(kg/m^3)**	**Young's Modulus (*E*)/(MPa)**	**Rigidity (*K*)/(N/m)**
0.45	0.45	0.015	0.6	0.001828	2200	30	2360

Table 3. Wave parameters.

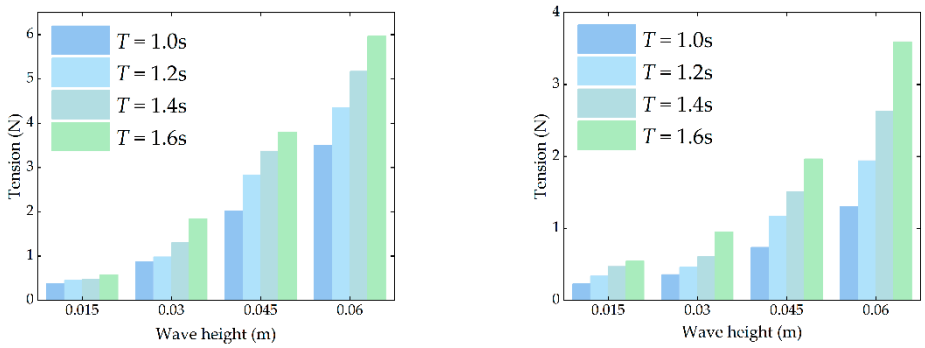
Water Depth (m)	Wave Height (m)	Period (s)
0.5	0.015, 0.03, 0.045, 0.06	1, 1.2, 1.4, 1.6

3.2.2. Influence of Different Wave Heights and Periods on the Floating Body Unit

To investigate the effects of wave heights and periods on the floating body unit, wave height H are set at 0.015 m, 0.03 m, 0.045 m, and 0.06 m. The periods T are set at 1 s, 1.2 s, 1.4 s, and 1.6 s. A total of 16 combinations of these conditions are established for numerical simulations. Where YL represents the numerical value of the mooring tension on the seaward side, BL represents the numerical value of the mooring tension on the leeward side.

Figure 8 shows the variation of the amplitude of the mooring force on both the seaward and leeward sides of the floating body unit with the wave height. As shown in Figure 8a, the mooring tension on the seaward side increases with both wave height and period. From Figure 8a, it is observed that the mooring tension on the seaward side increases with both wave height and period. Figure 9 presents the ratio of mooring tension on the seaward side to that on the leeward side at different wave heights. It also illustrates how this ratio changes with the wave period for a given wave height. It is evident that this ratio is greater than 1 across all wave heights. At a constant wave height, the ratio of tension decreases with increasing period. For instance, at H = 0.045 m, the maximum ratio YL/BL is 2.73, while the minimum YL/BL is 1.93. The primary reason for this behavior lies in the varying wave penetration capabilities associated with different wave periods. At the same water depth and wave height, shorter wave periods correspond to shorter wavelengths and poorer penetration capability, leading to higher relative energy dissipation as waves pass through the floating body unit. Consequently, the leeward line tension becomes significantly smaller than the seaward line tension under short periods. As the wave period increases, the wavelength lengthens, improving penetration capability, and reducing the relative energy dissipation. This results in a decrease in the YL/BL ratio. Figure 10 shows the amplitudes of surge, heave, and pitch of the floating body unit under different wave periods and heights. It is evident that as wave height and period increase, the amplitudes of all three motions also increase. According to Figure 10, the mooring tension of the floating body unit is primarily influenced by wave height. Surge is affected by both wave height and period, with wave height having a more significant impact. Heave is predominantly

influenced by wave height, with minimal impact from wave period. Pitch, on the other hand, is influenced by both wave height and period, with each factor having a relatively balanced effect.



(**a**) (**b**)

Figure 8. Influence of wave height on the mooring tension: (**a**) seaward line, (**b**) leeward line.

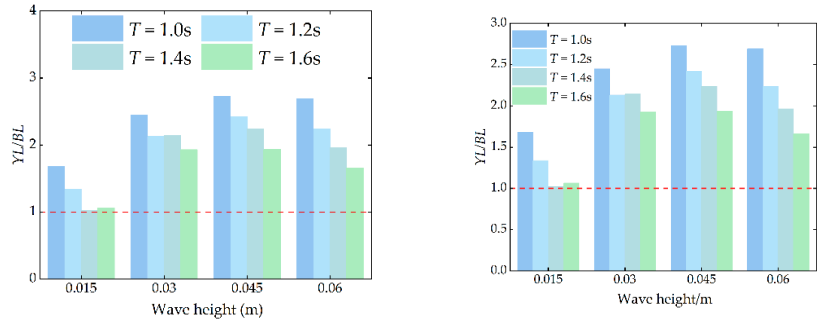
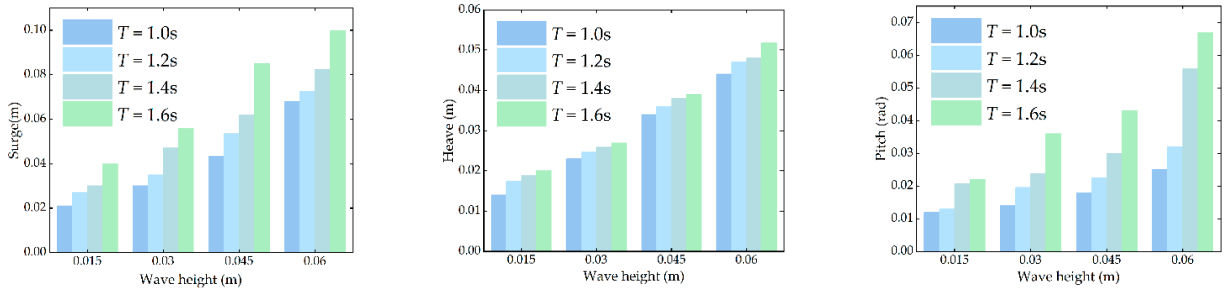


Figure 9. Influence of wave height on the ratio of mooring tension on the front side to that on the back side.



(**a**) (**b**) (**c**)

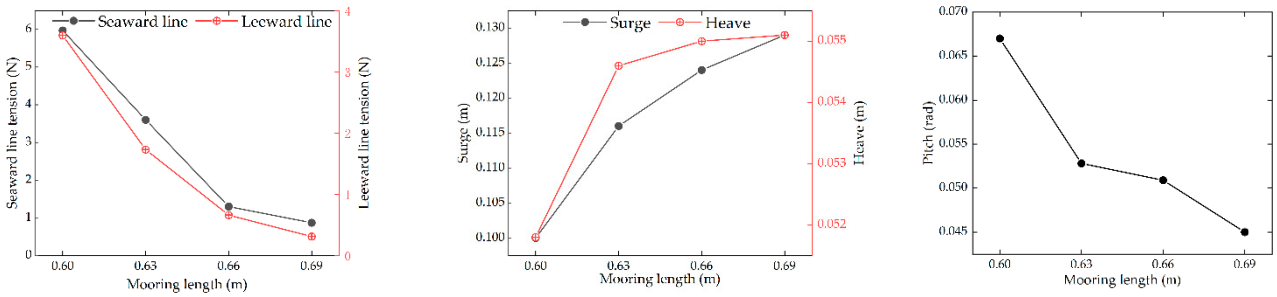
Figure 10. Influence of wave height on the amplitude of three-degree-of-freedom motion of floating body unit: (**a**) surge, (**b**) heave, (**c**) pitch.

3.2.3. Influence of Mooring Length

This section investigates the effect of mooring length on the floating body unit by conducting numerical simulations under conditions of a wave height of 0.06 m and a period of 1.6 s. The mooring lengths considered are 0.6 m, 0.63 m, 0.66 m, and 0.69 m.

Figure 11a illustrates the effect of mooring length on the mooring tension on both the seaward and leeward sides of the floating body unit. The results show that as the mooring length increases, both the seaward and leeward mooring tensions gradually decrease and stabilize. This behavior can be attributed to the increased contact area between the mooring line and the bottom of the flume as the mooring length increases. A longer mooring line generates pressure and friction at the flume bottom due to its self-weight, which reduces

the mooring tension. Furthermore, as the mooring line length increases, the effective length of the mooring line acting on the floating body unit becomes shorter. When the mooring line reaches 0.66 m, it approaches the vertical distance between the floating body unit and the flume bottom. Beyond this point, further increases in mooring length result in diminishing changes in mooring tension. Figure 11b,c illustrate the impact of mooring line length on the amplitudes of surge, heave, and pitch of the floating body unit. It is evident that as the mooring line length increases, the surge amplitude decreases, while the amplitudes of heave and pitch increase. Surge is primarily influenced by wave forces and horizontal mooring tension. Under constant wave conditions, a longer mooring line forms a larger angle with the horizontal direction at the connection point to the floating body unit, leading to reduced horizontal forces and a decrease in surge amplitude. As the mooring line length increases, larger bending and natural sagging regions develop in the water, resulting in higher vertical forces acting on the floating body unit. This causes a reduction in pitch amplitude and an increase in heave amplitude. However, once the length of the mooring line acting on the floating body unit stabilizes, the angle approaches approximately 90°, resulting in diminishing changes to the heave amplitude.

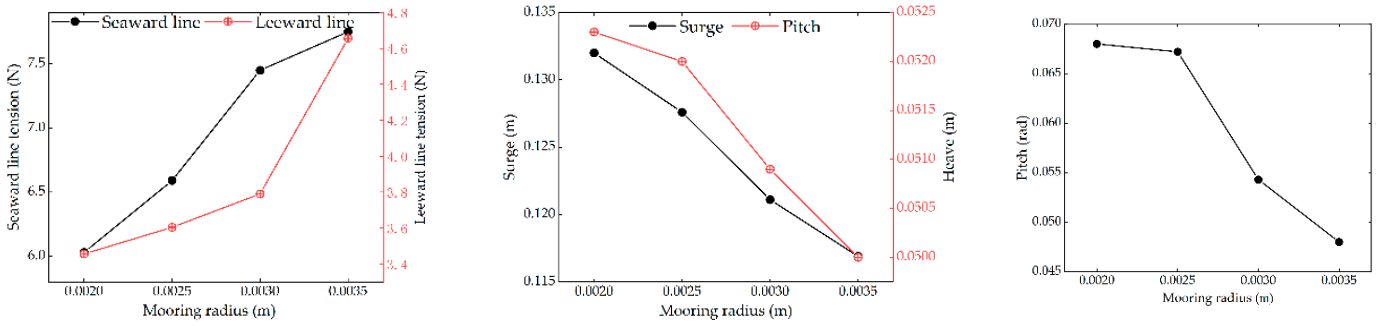


(**a**) (**b**) (**c**)

Figure 11. The influence of mooring line length on mooring tension, surge, heave, and pitch motion of floating unit is studied: (**a**) mooring tension, (**b**) surge and heave, (**c**) pitch.

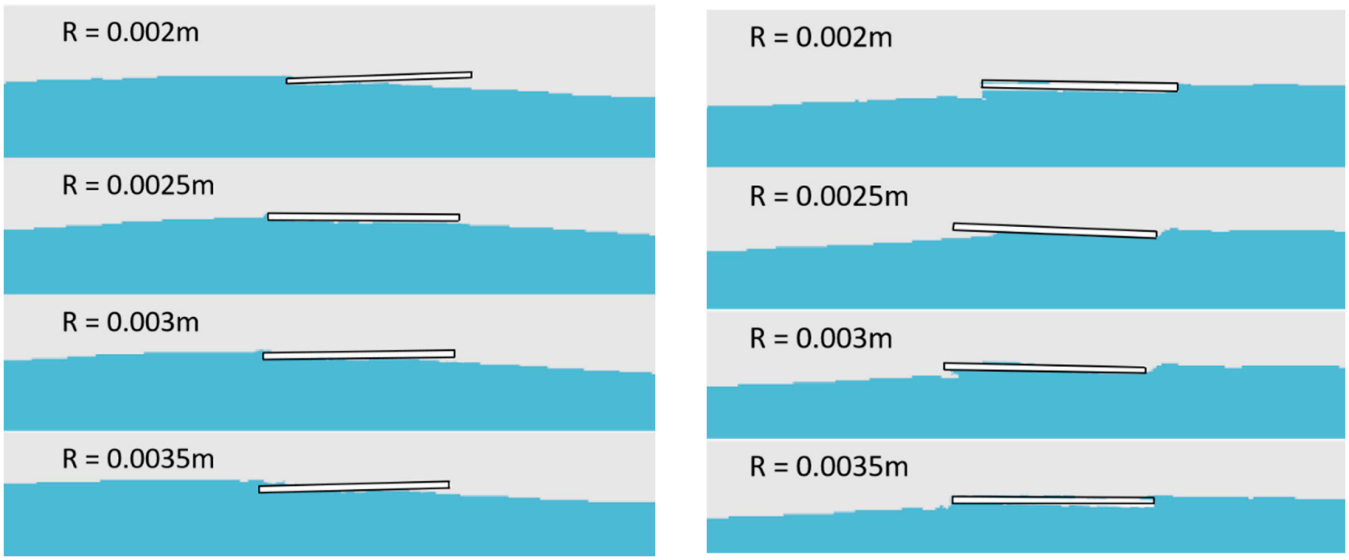
3.2.4. Influence of Mooring Radius

This section investigates the impact of mooring line radius on the floating body unit through numerical simulations conducted under conditions of a wave height of 0.06 m and a period of 1.6 s. The mooring line radius is set at 0.002 m, 0.0025 m, 0.003 m, and 0.0035 m. Figure 12a illustrates the effect of mooring line radius on the mooring tension. The results show that as the mooring line radius increases, both the seaward and leeward mooring tensions gradually increase. This can be attributed to the increased mass of the mooring line with a larger radius, which subsequently enhances the tension on the floating body unit. Figure 12b,c depict the influence of mooring line radius on the amplitudes of surge, heave, and pitch motions of the floating body unit. It is evident that as the mooring line radius increases, the amplitudes of these motions decrease, which is consistent with the findings of Liu B [38] and Song J [39]. Figure 13 shows the motion diagram of the floating body unit in a cycle. Figure 13a is the state where the floating body unit is located on the rightmost side, and Figure 13b is the state where the floating body unit is located on the leftmost side. The increase in mooring line radius not only increases the mass of the mooring line but also provides a greater restoring force, making the mooring line less susceptible to deformation. This results in enhanced stability and limits the motion of the floating body unit. This can be well demonstrated from Figure 13.



(a) (b) (c)

Figure 12. Influence of mooring tension, surge, heave, and pitch motion amplitude of mooring line radius floating body unit: (**a**) mooring tension, (**b**) surge and heave, (**c**) pitch.



(a) (b)

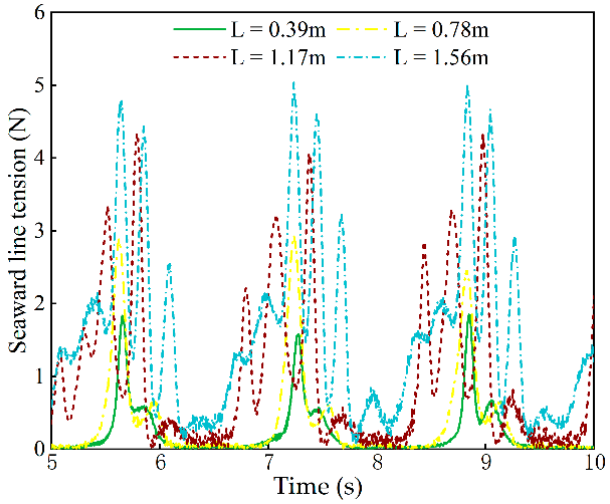
Figure 13. Motion state of floating body unit: (**a**) floating body unit moving to the right limit, (**b**) floating body unit moving to the left limit.

3.2.5. Influence of Floating Body Unit Length

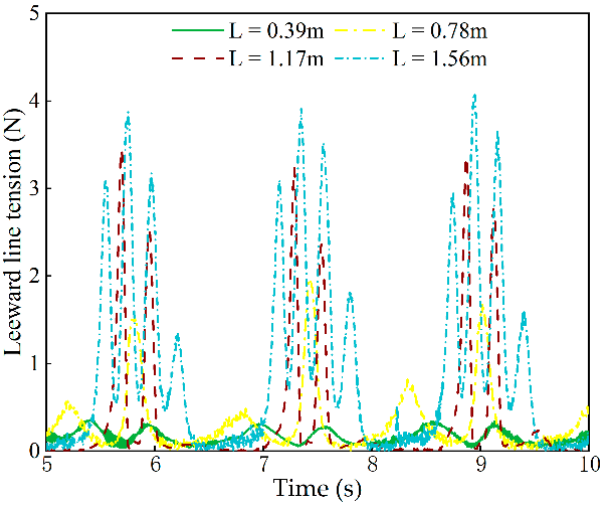
In this section, the influence of the floating body unit's length on its hydrodynamic forces is investigated through numerical simulations conducted under conditions of a wave height of 0.06 m and a period of 1.6 s. The length of the floating body unit is varied, with values set at 0.39 m, 0.78 m, 1.17 m, and 1.56 m. Figure 14 illustrates the variation of mooring tension with respect to the floating body unit's length, along with the time-history curves of surge, pitch, and heave motions.

From Figure 14a, it is evident that as the plate length increases, the mooring force on the wave-facing side gradually rises. For L = 0.39 m, the secondary peak of the mooring force is relatively small. When L = 0.78 m, the main peak increases significantly, and the secondary peak becomes more pronounced. At L = 1.17 m, the force exhibits four peaks within one cycle, with the peak values increasing initially and then decreasing. For L = 1.56 m, the cycle further develops six peaks, following the same trend of initial increase and subsequent decrease in peak values. Figure 14b shows that with increasing plate length, the anchor chain force on the back-wave side follows a similar trend to that on the wave-facing side. For L = 0.39 m, there are two small peaks. When L = 0.78 m, the main peak grows substantially, while the secondary peak shows a moderate increase. For

L = 1.17 m, both the main and secondary peaks increase significantly. When L = 1.56 m, the force cycle presents four distinct peaks. Figure 14c shows that, for lengths between 0.39 m and 0.78 m, the surge motion amplitude decreases, and the secondary peak value diminishes. However, between lengths of 0.78 m and 1.17 m, the surge motion amplitude increases by an average of 113%, with a pronounced growth rate. The secondary peak disappears, and the primary peak becomes smoother. Figure 14d reveals that, as the length of the floating body unit increases, the pitch amplitude first increases and then decreases. The largest pitch amplitude occurs when the length reaches 1.17 m. Figure 14e shows that the heave motion amplitude decreases gradually with increasing length. A secondary peak appears when the length is 0.78 m, and this secondary peak gradually diminishes as the length further increases.

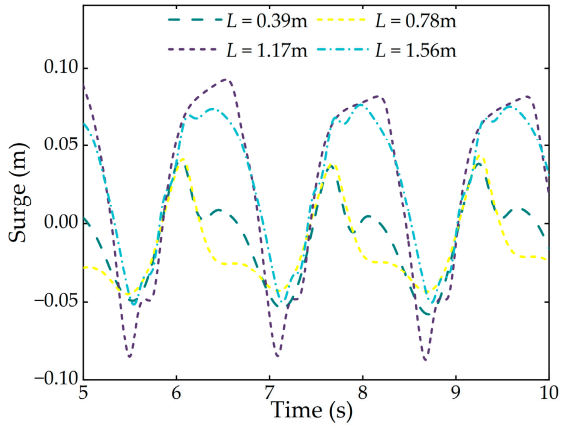


(**a**)

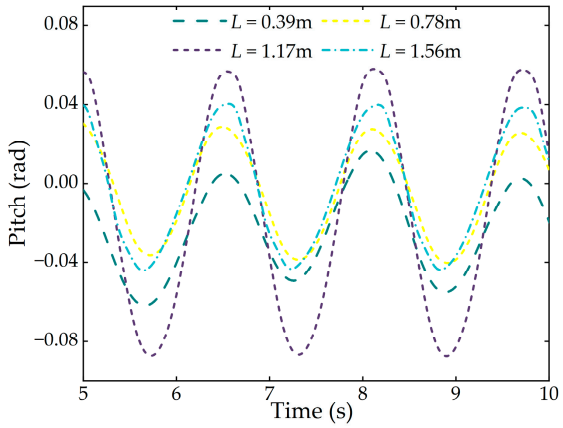


(**b**)

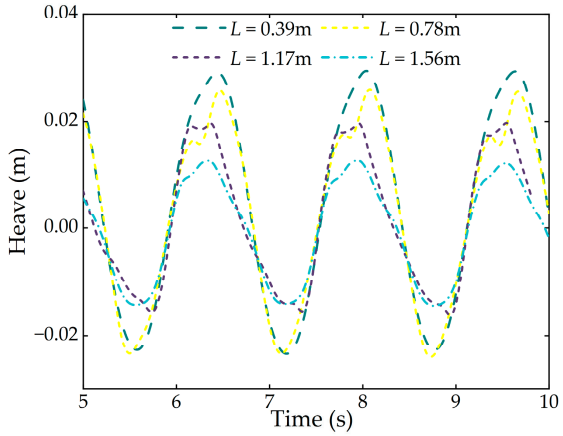
Figure 14. *Cont.*



(**c**)



(**d**)



(**e**)

Figure 14. Effects of different floating body unit lengths on the mooring tension, surge, pitch, and heave motions of the floating body unit: (**a**) seaward line tension, (**b**) leeward line tension, (**c**) surge, (**d**) pitch, (**e**) heave.

3.2.6. Influence of the Number of Different Floating Body Units

When the length L of the floating body unit is fixed, varying the number of floating body units can alter the total length D of the single-row array, thereby affecting the mooring tension and motion responses of the array. This section investigates the impact of the number of floating body units on the mooring tension and motion responses under conditions of wave heights H = 0.060 m and H = 0.045 m, a period T = 1.6 s, and a wavelength λ = 3.09 m. The number of floating body units is set to 3, 6, 9, and 12, with a unit length L = 0.45 m and a spacing of 0.06 m, resulting in total length D = 1.47 m, 3 m, 4.53 m, and 6.06 m. The arrangement of floating body unit is shown in Figure 15. As shown in Figure 16, the connection between floating body units is achieved through spherical hinges, which do not allow for horizontal relative displacement between the units. The relative total length is defined as the ratio of the total length D of the floating array to the wavelength λ, approximately D/λ of 0.5, 1, 1.5, and 2.

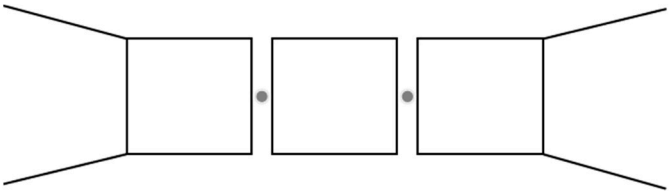


Figure 15. Schematic diagram of floating unit arrangement (with D/λ = 0.5 as an example).

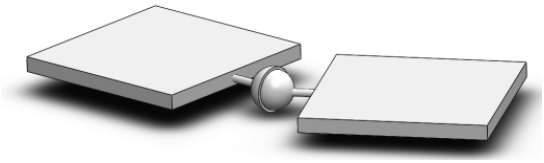
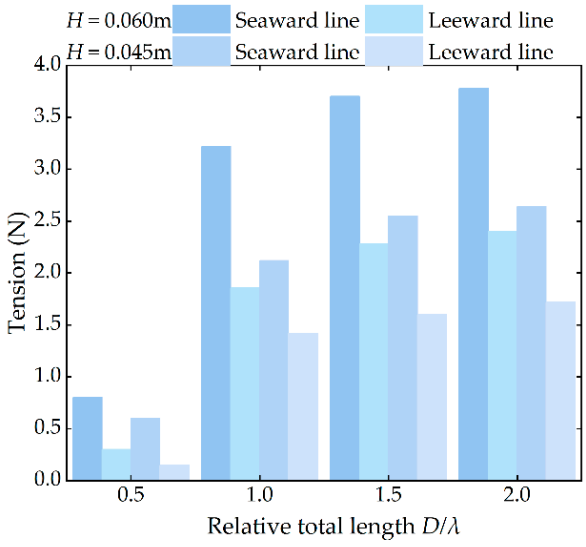


Figure 16. Spherical hinge diagram.

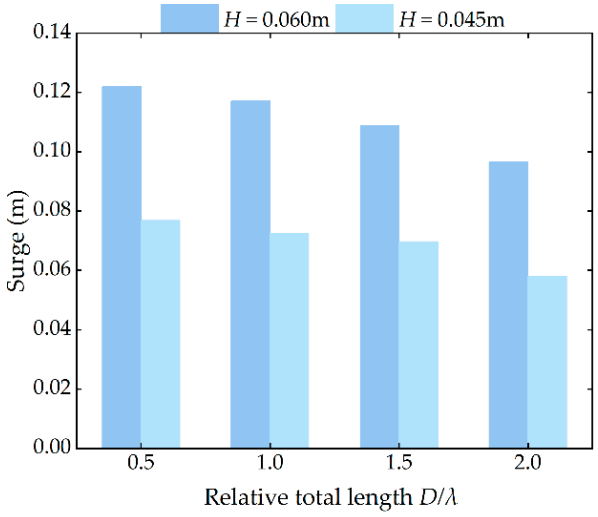
Figure 17 presents the mooring tension and motion responses of photovoltaic arrays at different relative total lengths D/λ in wave conditions. From Figure 17a, it can be observed that as the relative total length D/λ increases, both the seaward mooring tension and leeward mooring tension show an increasing trend. As the wave height increases, the mooring tension also increases. The mooring tension on the seaward line is always greater than the leeward line, which is consistent with the floating body unit. When D/λ = 0.5, there is a significant difference in mooring tension compared to D/λ = 1, D/λ = 1.5, and D/λ = 2. However, there is little difference in the numerical values of mooring tension between the seaward side and the leeward side when D/λ = 1, D/λ = 1.5, and D/λ = 2. Due to the articulated connections, horizontal relative displacement between the floating body units is not permitted, resulting in nearly identical surge motion amplitudes for each unit. Therefore, Figure 17b shows the change of the average surge motion amplitude with the relative total length D/λ. It can be seen that the surge motion amplitude decreases as the relative total length increases, although the decrease is small. When H = 0.060 m, the average decrease is 5.5%, and when H = 0.045 m, the average decrease is 4.7%. From Figure 17c, it is evident that the pitch amplitude for H = 0.060 m is greater than that for H = 0.045 m. As the relative total length D/λ increases, the pitch motion amplitudes of the floating body units generally decrease for both wave heights, except for unit number 5. Moving from the seaward side to the leeward side, the pitch motion amplitude of the photovoltaic array shows a decreasing trend with increasing unit number. However, due to the tension exerted by the mooring on one side of the array, the floating body units connected to the mooring experience larger pitch angles, with maximum pitch angles of 0.18 rad and 0.15 rad, respectively. Therefore, in practical engineering applications,

reinforcement measures should be implemented for the floating body units on both sides to prevent structural damage from excessive pitch motion. It can be seen from Figure 17d that from the seaward side to the leeward side, H = 0.060 m is slightly larger than H = 0.045 m and shows the same trend. The pitch motion of the photovoltaic array with a relative total length of D/λ = 0.5 exhibits a decreasing trend, while for D/λ = 1, the pitch motion first decreases and then increases. For D/λ = 1.5, the pitch motion initially decreases, then increases, and finally decreases again. For D/λ = 2, the pitch motion shows a trend of decrease, increase, decrease, and finally increase. Regardless of the number of floating body units in the array, units of the same index exhibit similar trends with increasing relative total length. It is hypothesized that floating body units 1, 2, 3, 7, 8, and 9 are primarily affected by the gradual dissipation of wave energy on the seaward side and the fixed mooring effect, resulting in a decreasing heave amplitude. In the photovoltaic array with six floating body units, the varying forces exerted by the waves on both sides of the mooring lead to differences in the angles relative to the horizontal. The seaward side forms a smaller angle with the horizontal compared to the leeward side, resulting in an increase in heave amplitude on the leeward side. In the array with nine floating body units, the larger number of units creates a compressive effect on the central units, combined with the fixed ends and the self-weight of the floating body units, resulting in greater inertia for the central units. Therefore, the heave motion amplitude of floating body units with serial numbers 4, 5, and 6 increases. As the relative total length D/λ increases, the heave motions of the floating body units connected to both the seaward and leeward mooring lines show a decreasing trend. In the photovoltaic array with 12 floating body units, the motion amplitude of the floating body units with serial numbers of 10, 11, and 12 gradually increases due to the traction of the mooring on the leeward side. Therefore, in practical applications, an excessive number of floating body units may cause significant heave motion at the center of the floating body array, potentially leading to the failure of connections between the units in that area.

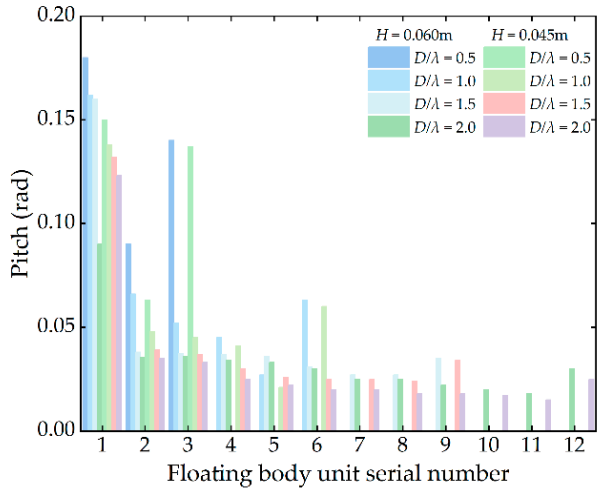


(**a**)

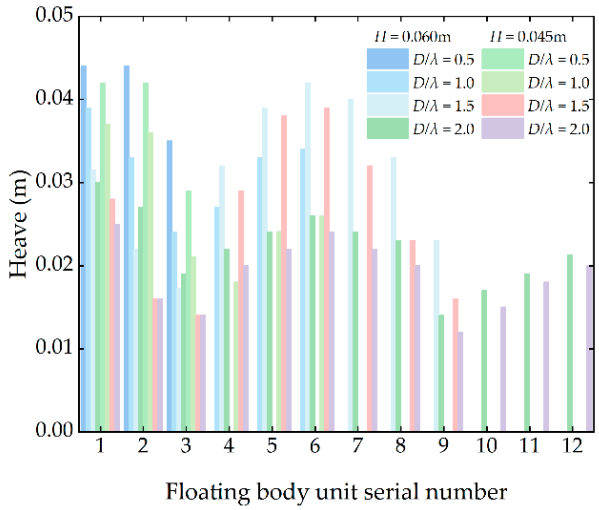
Figure 17. *Cont.*



(**b**)



(**c**)



(**d**)

Figure 17. The mooring tension and the amplitude of surge, pitch, and heave motion of floating body units with different relative total lengths are analyzed: (**a**) change of mooring tension with relative total length; (**b**) variation of average surge motion amplitude with relative total length; (**c**) pitching motion amplitude of floating body unit at different positions; (**d**) heave motion amplitude of the floating body unit at different positions.

4. Conclusions

This paper establishes a numerical model for the discrete element method (DEM) mooring based on viscous flow numerical simulation, aimed at exploring the effects of various wave parameters, length of floating body unit, and mooring parameters on the floating body unit, as well as the influence of different numbers of floating body units on the single-row floating body array. The main conclusions are summarized as follows:

1. The mooring tension, surge, and heave motion of the floating body unit are primarily affected by the wave height. Heave motion exhibits a strong linear relationship with wave height. For every 0.015 m increase in wave height, the amplitude of the heave motion increases by 0.01 m. The pitch motion is influenced by both wave height and period in a more balanced manner. As the period increases, the ratio of mooring tension on the seaward side to that on the leeward side gradually decreases, with the minimum ratio being 1.019.
2. Under the conditions presented in this paper, when the mooring length reaches 0.66 m (when the effective mooring length acting on the floating body unit approaches the vertical distance between the floating body unit and the bottom of the flume), the mooring tension and motion response of the photovoltaic panel tend to stabilize. Properly increasing the mooring line radius can effectively suppress the motion response of the floating body unit. Additionally, when the length of the floating body unit is 0.4 times the wavelength, the motion response becomes more intense.
3. In the floating body array, the number of floating body units and their spatial positions significantly influence the hydrodynamic performance. When the total length of the floating body array reaches one wavelength, increasing the number of floating body units has little effect on the mooring tension. When the length of the floating body array is 1.5 times the wavelength, the compressive effect exerted by the floating body units on the central units becomes more pronounced. The number of floating body units also has little impact on surge motion. The longer the floating body array, the smaller the motion response of the floating body units connected to the mooring.

The primary limitation of this paper lies in the use of a numerical simulation model based on a square thin plate composed of rigid materials and an array of such plates. As a result, it may not fully capture the motion characteristics of offshore floating photovoltaics made from flexible materials. Additionally, this study focuses exclusively on single-row floating body arrays, without exploring double-row or multi-row configurations. Therefore, in the subsequent work, the hydrodynamic characteristics of the 2D offshore floating photovoltaics will be studied.

Author Contributions: Conceptualization, S.S. and L.C.; methodology, S.S.; software, S.S.; validation, S.S.; formal analysis, S.S.; investigation, S.S.; resources, L.C.; data curation, S.S.; writing—original draft preparation, S.S.; writing—review and editing, S.S., Q.C. and Y.G.; visualization, Z.H.; supervision, L.C.; project administration, L.C.; funding acquisition, L.C. All authors have read and agreed to the published version of the manuscript.

Funding: This research was funded by the National Natural Science Foundation of China (grant no. 51909237) and project of Zhoushan Science and Technology Bureau (grant no. 2021C2013).

Data Availability Statement: The data used to support the findings of this study are included within the article.

Conflicts of Interest: The authors declare no conflict of interest.

References

1. Rehman, S.; Irshad, K.; Mohandes, M.A.; Al-Shaikhi, A.; Zayed, M.E. Comprehensive evaluation of solar floating photovoltaic prospective in Saudi Arabia: Comparative experimental investigation and thermal performance analysis. *Sol. Energy* **2024**, *283*, 113015. [CrossRef]
2. Kim, H.S.; Kim, B.W.; Hong, S.Y.; Lee, K. Dynamic Analysis on Module Type Floating Structure Consisting of Highly Numerous Buoys and Connection Beams. In Proceedings of the ISOPE International Ocean and Polar Engineering Conference, Sapporo, Japan, 10 June 2018; ISOPE: Mountain View, CA, USA, 2018; ISOPE-I-18-261.
3. Ikhennicheu, M.; Danglade, B.; Pascal, R.; Arramounet, V.; Trébaol, Q.; Gorintin, F. Analytical method for loads determination on floating solar farms in three typical environments. *Sol. Energy* **2021**, *219*, 34–41. [CrossRef]
4. Ranjbaran, P.; Yousefi, H.; Gharehpetian, G.; Astaraei, F.R. A review on floating photovoltaic (FPV) power generation units. *Renew. Sustain. Energy Rev.* **2019**, *110*, 332–347. [CrossRef]
5. Yousuf, H.; Khokhar, M.Q.; Zahid, M.A.; Kim, J.; Kim, Y.; Cho, E.C.; Cho, Y.H.; Yi, J. A review on floating photovoltaic technology (FPVT). *Curr. Photovolt. Res.* **2020**, *8*, 67–78.
6. Cazzaniga, R.; Rosa-Clot, M. The booming of floating PV. *Solar Energy* **2021**, *219*, 3–10. [CrossRef]
7. Jin, Y.; Zeng, Z.; Chen, Y.; Xu, R.; Ziegler, A.D.; Chen, W.; Ye, B.; Zhang, D. Geographically constrained resource potential of integrating floating photovoltaics in global existing offshore wind farms. *Adv. Appl. Energy* **2024**, *13*, 100163. [CrossRef]
8. Golroodbari, S.Z.; van Sark, W. Simulation of performance differences between offshore and land-based photovoltaic systems. *Prog. Photovolt. Res. Appl.* **2020**, *28*, 873–886. [CrossRef]
9. Vyas, M.; Chowdhury, S.; Verma, A.; Jain, V. Solar Photovoltaic Tree: Urban PV power plants to increase power to land occupancy ratio. *Renew. Energy* **2022**, *190*, 283–293. [CrossRef]
10. Trapani, K.; Millar, D.L. The thin film flexible floating PV (T3F-PV) array: The concept and development of the prototype. *Renew. Energy* **2014**, *71*, 43–50. [CrossRef]
11. Shaw, R.; Surjan, A.; Parvin, G.A. *Urban Disasters and Resilience in Asia*; Butterworth-Heinemann: Waltham, MA, USA, 2016.
12. Dai, J.; Zhang, C.; Lim, H.V.; Ang, K.K.; Qian, X.; Wong, J.L.H.; Tan, S.T.; Wang, C.L. Design and construction of floating modular photovoltaic system for water reservoirs. *Energy* **2020**, *191*, 116549. [CrossRef]
13. Luo, W.; Zhang, X.; Tian, X.; Cheng, Z.; Wen, B.; Li, X.; Luo, Y. Conceptual design and model test of a pontoon-truss type offshore floating photovoltaic system with soft connection. *Ocean Eng.* **2024**, *309*, 118518. [CrossRef]
14. Ji, C.; Gao, X.; Xu, S. Study on the influence of connector designs on the hydrodynamic performance of an offshore floating photovoltaic. *Ocean Eng.* **2024**, *308*, 118298. [CrossRef]
15. Jiang, Z.; Dai, J.; Saettone, S.; Tørå, G.; He, Z.; Bashir, M.; Souto-Iglesias, A. Design and model test of a soft-connected lattice-structured floating solar photovoltaic concept for harsh offshore conditions. *Mar. Struct.* **2023**, *90*, 103426. [CrossRef]
16. Wang, B.; Li, Y.; Huang, L.; Yao, Y.; Qin, Y. Dynamic analysis of a novel star-type floating photovoltaic system with flexible connectors. *Ocean Eng.* **2024**, *304*, 117854. [CrossRef]
17. Li, Y.; Li, G.; Cui, Y.; Deng, W.; Wang, B.; Li, H.; Feng, Y.; Meng, H. The influence of multi-body interaction on the hydrodynamic performance of a hexagon-type floating photovoltaic. *Ocean Eng.* **2024**, *312*, 119302. [CrossRef]
18. Xu, W.; Sun, Y.; He, Z. Hydrodynamic performance study of floating photovoltaic arrays with multiple floating bodies. *Appl. Ocean Res.* **2024**, *153*, 104286. [CrossRef]
19. Tang, Y.; Chen, X.; Huang, G.; Chen, M.; Zhang, K.; Jiang, Y.; Li, T.; Tao, T.; Yang, Y. Dynamic analysis of multi-module floating photovoltaic platforms with composite mooring system by considering tidal variation and platform configuration. *Ocean Eng.* **2024**, *312*, 119243. [CrossRef]
20. Du, J.; Zhang, D.; Zhang, Y.; Xu, K.; Chang, A.; Zhao, S. Design and comparative analysis of alternative mooring systems for offshore floating photovoltaics arrays in ultra-shallow water with significant tidal range. *Ocean Eng.* **2024**, *302*, 117649. [CrossRef]
21. Lu, Y.; Chen, H.; Tomac, I.; McCartney, J.S. Analytical and numerical investigation of gravity anchors for floating photovoltaic systems. *Ocean. Eng.* **2024**, *313*, 119591. [CrossRef]
22. Hou, Y.; Zhao, X.; Tao, G.; Huang, Z.; Xu, N.; Leng, Z. Study on the Characteristics of Flow over a Seawall and Its Impact on Pedestrians under Solitary Wave Action. *Water* **2024**, *16*, 2357. [CrossRef]
23. Song, Z.; Jiao, Z.; Gao, J.; Mi, C.; Liu, Y. Numerical investigation on the hydrodynamic wave forces on the three barges in proximity. *Ocean Eng.* **2025**, *316*, 119941. [CrossRef]
24. Zhao, X.; Hou, Y.; Lu, F.; Shi, Z.; Huang, Z. Numerical investigations of pedestrian overboard on a compound slope dike due to excessive overtopping waves. *Phys. Fluids* **2024**, *36*, 107148. [CrossRef]
25. Domínguez, J.M.; Crespo, A.J.; Hall, M.; Altomare, C.; Wu, M.; Stratigaki, V.; Peter, T.; Lorenzo, C.; Moncho, G.G. SPH simulation of floating structures with moorings. *Coast. Eng.* **2019**, *153*, 103560. [CrossRef]
26. Chen, H.; Hall, M. CFD simulation of floating body motion with mooring dynamics: Coupling MoorDyn with OpenFOAM. *Appl. Ocean Res.* **2022**, *124*, 103210. [CrossRef]

27. Mi, C.; Gao, J.; Song, Z.; Liu, Y. Hydrodynamic wave forces on two side-by-side barges subjected to nonlinear focused wave groups. *Ocean Eng.* **2025**, *317*, 120056. [CrossRef]
28. Gao, J.; Mi, C.; Song, Z.; Liu, Y. Transient gap resonance between two closely-spaced boxes triggered by nonlinear focused wave groups. *Ocean Eng.* **2024**, *305*, 117938. [CrossRef]
29. Gong, S.; Gao, J.; Song, Z.; Shi, H.; Liu, Y. Hydrodynamics of fluid resonance in a narrow gap between two boxes with different breadths. *Ocean Eng.* **2024**, *311*, 118986. [CrossRef]
30. Gao, J.-L.; Lyu, J.; Wang, J.-H.; Zhang, J.; Liu, Q.; Zang, J.; Zou, T. Study on transient gap resonance with consideration of the motion of floating body. *China Ocean Eng.* **2022**, *36*, 994–1006. [CrossRef]
31. Wang, W.; Gao, Z. A dynamical remeshing-based explicit lumped mass method for damaged ship flooding dynamics. *Ocean Eng.* **2025**, *317*, 120075. [CrossRef]
32. Liu, H.; Zhou, B.; Han, X.; Zhang, T.; Zhou, B.; Gho, W.M. Numerical simulation of water entry of an inclined cylinde. *Ocean. Eng.* **2020**, *215*, 107908. [CrossRef]
33. Zhou, B.; Liu, H.; Wu, Z.; Han, X.; Sun, T.; Zhang, G. Numerical Study of Vertical Water Entry of Cylinder under the Influence of Wind and Current. *Phys. Fluids* **2021**, *33*, 033330. [CrossRef]
34. Zhu, Y. Analyses of the ranges of validity for several wave theories. *Coast. Eng.* **1983**, *2*, 11–27.
35. Liang, J.-M.; Liu, Y.; Chen, Y.-K.; Li, A.-J. Experimental study on hydrodynamic characteristics of the box-type floating breakwater with different mooring configurations. *Ocean Eng.* **2022**, *254*, 111296. [CrossRef]
36. Chen, H.; Medina, T.A.; Cercos-Pita, J.L. CFD simulation of multiple moored floating structures using OpenFOAM: An open-access mooring restraints library. *Ocean Eng.* **2024**, *303*, 117697. [CrossRef]
37. Du, W. Wave Characteristics and Wave Energy Prediction in the East China Sea. Master's Thesis, Ludong University, Yantai, China, 2023.
38. Liu, B.; Yu, J. Effect of Mooring Parameters on Dynamic Responses of a Semi-Submersible Floating Offshore Wind Turbine. *Sustainability* **2022**, *14*, 14012. [CrossRef]
39. Song, J.; Kim, J.; Chung, W.C.; Jung, D.; Kang, Y.J.; Kim, S. Wave-induced structural response analysis of the supporting frames for multiconnected offshore floating photovoltaic units installed in the inner harbor. *Ocean Eng.* **2023**, *271*, 113812. [CrossRef]

Disclaimer/Publisher's Note: The statements, opinions and data contained in all publications are solely those of the individual author(s) and contributor(s) and not of MDPI and/or the editor(s). MDPI and/or the editor(s) disclaim responsibility for any injury to people or property resulting from any ideas, methods, instructions or products referred to in the content.